

# Hybrid-Size Quantum Dots in Hole Transport Layer Depress Dark Current Density of Short-Wave Infrared Photodetectors

Simin Chen,<sup>△</sup> Huaying Zhong,<sup>△</sup> Xiao Wang,<sup>△</sup> Guangjiu Pan, Haodong Tang,\* Fan Fang, Jiufeng Wu, Weichao Wang, Lihai Xu, Jun Tang, Junjie Hao, Keyu Zheng, Dan Wu, Zeguo Tang, Lei Zhang, Leifeng Cao, Peter Müller-Buschbaum,\* Kai Wang,\* and Wei Chen\*



Cite This: *ACS Photonics* 2025, 12, 879–888



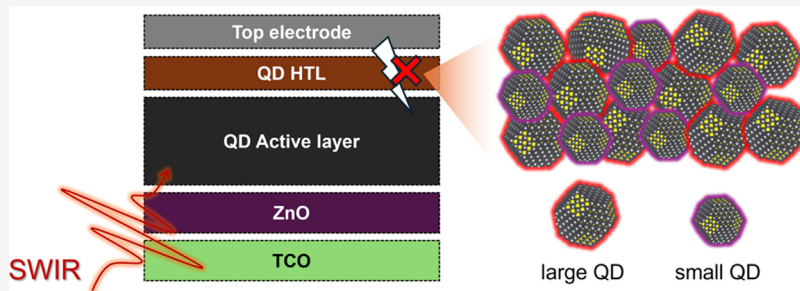
Read Online

ACCESS |

Metrics & More

Article Recommendations

Supporting Information



**ABSTRACT:** PbS quantum dots (QDs) are promising materials for low-cost short-wave infrared (SWIR) photodetection and imaging applications, owing to their unique optical properties and tunable bandgap. High-performance photodiodes rely on thiol-treated small PbS QDs as the hole transport layer (HTL) due to their suitable band alignment, but they face challenges such as crack formation, which increases dark currents. We develop a crack-free HTL by mixing small-size and large-size QDs. Grazing incidence small-angle X-ray scattering data confirms that the hybrid-size QD HTL is more homogeneous and denser than that made from monosize QDs. Photophysical studies show optimized charge carrier dynamics and energy transfer in the hybrid-size QDs, compared to monosize QDs. The devices based on the hybrid-size QD HTL exhibit a significantly reduced dark current density ( $392 \text{ nA/cm}^2$ ). Additionally, they show high device performance, including a responsivity of  $0.65 \text{ A/W}$ , detectivity of  $2.4 \times 10^{12} \text{ Jones}$ , and an external quantum efficiency of 65% in the SWIR region, paving the way for high-performance QD-based SWIR photodetectors.

**KEYWORDS:** quantum dots, hybrid-size, hole transport layer, GISAXS

## INTRODUCTION

Quantum dots (QDs) are regarded as a magic material in many optoelectronic applications, including light-emitting diodes (LEDs),<sup>1,2</sup> solar cells, and photodetectors,<sup>3–7</sup> primarily due to their tunable bandgap, which can be adjusted by changing their size, as well as their solution processability, which enables low-cost fabrication. Specifically, lead sulfide (PbS) QDs are particularly promising in short-wave infrared (SWIR) photodetectors due to the naturally narrow bandgap and suitable charge carrier diffusion length (<300 nm) of the solid films.<sup>8,9</sup> The limited charge carrier diffusion length of the QD solid films enables high-resolution QD imaging through monolithic QD deposition on CMOS chips, offering a significantly lower cost compared to the traditional InGaAs SWIR technique, which relies on a “flip-chip” process.<sup>10–12</sup>

Presently, to fabricate highly efficient photodiode devices, such as solar cells and SWIR photodetectors, thiol-treated QD layers are commonly used as hole transport layers (HTLs) due to their favorable band alignment and the formation of a “homojunction” with a lower energy barrier for charge carrier

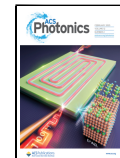
transfer between the QD active layer and the QD HTL.<sup>13,14</sup> The fabrication process of the QD HTL is known as a solid-state ligand exchange (SSLE) as described below.<sup>15,16</sup> Organic-capped QDs, such as those with long-chain ligands like oleic acid (OA), tend to form a superlattice due to their inherent propensity for long-range ordered stacking through self-assembly. A short-chain thiol precursor is consequently applied to the pristine QD film to initiate the SSLE, during which all long-chain ligands of the QDs are simultaneously substituted by thiol ligands. A 2- or 3-step rinsing process is then applied to remove any residual long-chain ligands, though this inevitably leads to crack formation due to the volume contraction of the QD ensemble.<sup>17</sup> The deposition process is

Received: September 27, 2024

Revised: December 19, 2024

Accepted: December 23, 2024

Published: January 2, 2025



**Scheme 1.** (a) Crack Formation Leads to the Leakage Current in QD HTLs with Monosize QDs and (b) QD HTLs with H-QDs are Crack-free in the Solid

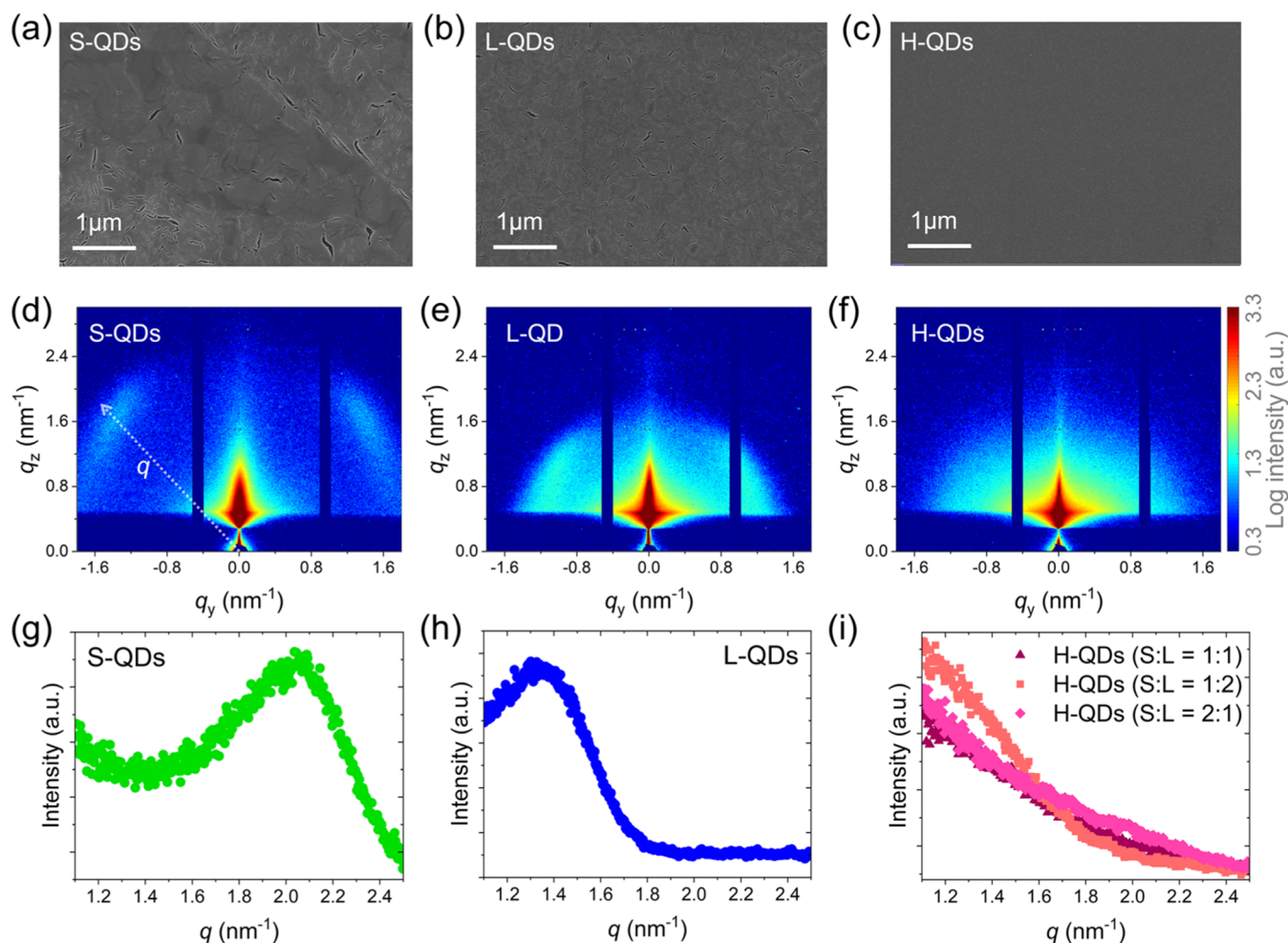
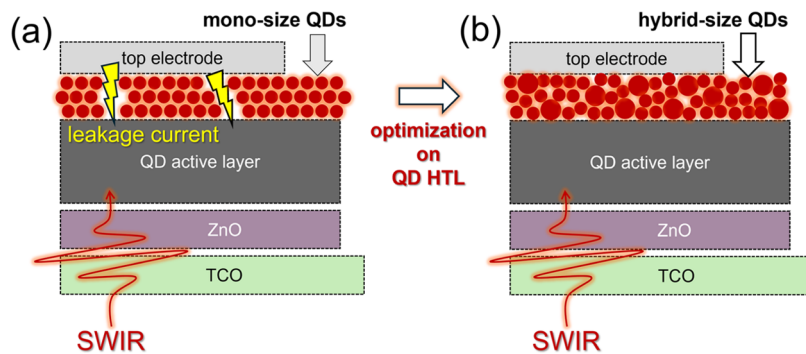


**Figure 1.** (a–c) SEM images of the QD HTLs, (d–f) 2D GISAXS data of QD HTLs made of different configurations in size, (g–i) corresponding azimuthal integrations of the 2D GISAXS data.

repeated two or three times to increase the layer thickness and partially refill the crack space.<sup>15</sup> After several hours of storage in dry air, the QD solid film demonstrates p-type semiconductor behavior and can be used as the HTL in QD diode devices.<sup>18,19</sup> Many factors, including the light conditions, ambient humidity, etc. during oxidation doping, can significantly affect QD-HTL performance and device efficiency.<sup>14,18</sup> Therefore, refining the QD HTL treatment in the oxygen doping process is crucial for achieving high-performance QD devices, in addition to ensuring the quality of other

functional layers and interfaces. Another challenge arises from structural modulation, as the final QD HTL often develops micrometer-scale cracks if not properly refilled during the SSLE process. Particularly monosize QDs exhibit a more pronounced crack formation, as indicated in Scheme 1a. These HTL cracks can further lead to unexpected contacts between the electrodes and the QD active layer, thus increasing the dark current density by introducing ohmic contacts. Many efforts in the literature have been implemented to reduce the crack formation of the QD HTLs. For instance, Wang et al.

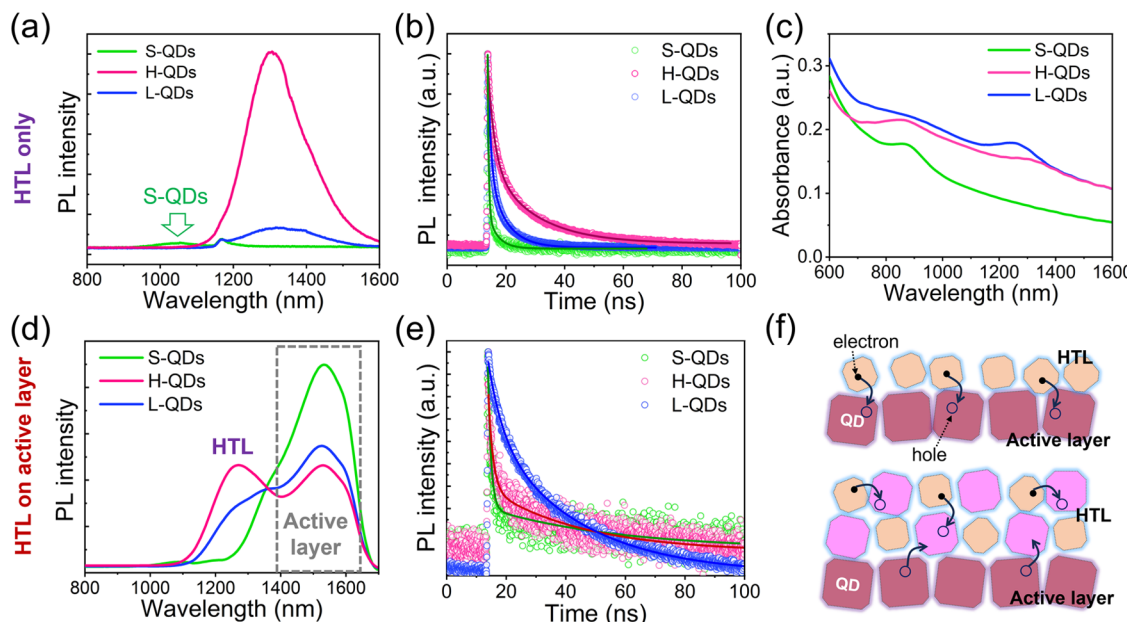


**Figure 2.** (a) PL spectra of QD HTLs on glass. (b) TR-PL data of the QD HTLs. (c) Absorption spectra of the QD HTLs. (d) PL spectra of the QD HTLs on the QD active layer. (e) TR-PL data of the QD active layer with different-size QD HTLs. (f) Schematic of charge carrier dynamics of monosize QD HTL (top) and hybrid-size QD HTL (bottom) on QD active layer.

developed a QD ink technique via a solution-processed ligand exchange process for the HTL fabrication and deposition, effectively decreasing the volume contraction and thus reducing the crack generation.<sup>20</sup> Sharma et al. used a pretreatment of the OA-PbS QDs reducing the cracks of the final HTL by changing the surface condition of the QDs.<sup>21</sup> Based on a similar principle, Huang et al. used a hybrid ligand exchange method by using MPA and EDT synergic ligands in the SSLE process and successfully reduced the cracks from the volume contraction.<sup>22</sup> These efforts highlight two key factors in the formation of crack-free QD HTLs. First, achieving a crack-free QD HTL can improve device performance by reducing leakage current. Second, modulating the stacking dynamics of QDs during the “liquid-to-solid” transition plays a crucial role in crack-free QD film formation.<sup>23–26</sup> Specifically, establishing a long-range disordered film configuration, such as by reducing uniform surface conditions or altering the nanoparticle morphology (e.g., by partially fusing the QDs), is considered an effective method for achieving optimized QD HTLs with crack-free morphologies.<sup>27</sup> The fundamental mechanism behind the crack-free optimization of SSLE-based QD solids is hypothesized to involve short-range disorder inducing long-range disorder. This process can lead to self-compensation for volume contraction by alleviating or releasing strain forces generated during the ligand exchange-induced structural phase transition. Furthermore, short-range disorder in the QDs can be established through self-assembly of multimodal distribution QDs,<sup>28,29</sup> with the ligand exchange treatment causing an isotropic collapse of the QD arrangement, avoiding crack formation.

Herein, we propose a simple and effective method by mixing QDs of two different sizes in the regular SSLE process to achieve crack-free QD HTL, as indicated in Scheme 1b. Scanning electron microscopy (SEM) characterizations verify that the cracks are significantly depressed in QD HTLs made of hybrid-size QDs (H-QDs). Moreover, the stacking kinetics of H-QDs are studied by grazing-incidence small-angle X-ray

scattering (GISAXS) revealing that short-range disorder leads to a long-range compact stacking configuration in the final QD HTL. We further study how short-range disorder improves the charge carrier dynamics in QD HTLs and devices through photophysical studies. As a result, QD SWIR photodetectors with H-QD HTLs exhibit significantly depressed dark current densities compared to the devices with monosize QD HTLs. Thus, using H-QDs in HTL fabrication is an effective method for fabricating highly efficient photodetectors and imagers.

## RESULTS AND DISCUSSION

To prepare H-QDs, two different sizes of QDs are selected from their absorption features. OA-capped QDs with the first exciton peak at 850 nm are denoted as small-size QDs (S-QDs). OA-capped QDs with the first exciton peak at 1350 nm are denoted as large-size QDs (L-QDs). The fabrication process of the QDs is seen in the experimental section. The morphologies and the absorption spectra of S-QDs and L-QDs are given in Figures S1 and S2.

After deposition and the SSLE process, the surface morphologies of the QD HTLs made of different-size QDs are illustrated in Figures 1(a–c) and S3. The SEM images suggest the apparent crack generation of the QD HTL made of monosize QDs (S-QDs and L-QDs), while the QD solids made of H-QDs are significantly improved and appear “crack-free” at the observation scale. Monosize QDs undergo substantial superlattice transformation due to the short-range order configuration,<sup>23</sup> particularly in the ligand exchange process,<sup>26</sup> where anisotropic volume contraction induces strong strain force and leads to crack formation. As mentioned in the introduction, the H-QDs can easily release the strain force due to the short-range disorder configuration. The stacking configuration of the QDs in the solids made of monosize QDs and H-QDs are respectively studied by GISAXS and the 2D GISAXS patterns are shown in Figure 1(d–f). In the cases of monosize QD solids, prominent Bragg scattering features can be observed in the out-of-the-plane

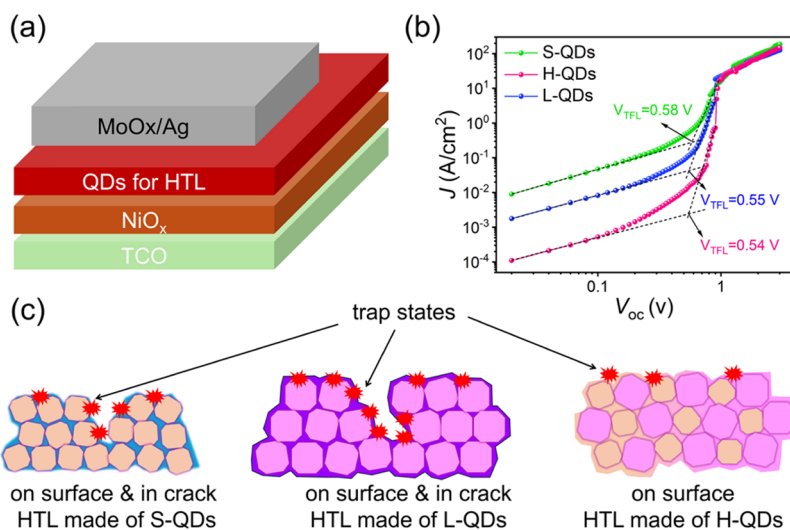


**Figure 3.** (a) Single charge carrier device architecture. (b)  $J$ – $V$  characteristics of the single charge carrier devices. (c) Schematic of trap states distribution in monosize QDs and hybrid-size QDs.

direction of the 2D GISAXS data in Figure 1(d,e), which suggests a uniformed interdot arrangement. No such structure configuration observed in H-QD solid from the GISAXS pattern in Figure 1(f). The corresponding azimuthal integrations to the GISAXS patterns of all QD solids are conducted according to previous literature,<sup>30,31</sup> and the results are shown in Figure 1(g–i). In reciprocal space, small QDs exhibit a larger  $q$  Bragg peak at  $q = 2.1 \text{ nm}^{-1}$  while the large QDs show the Bragg peak at a lower  $q$  position,  $q = 1.3 \text{ nm}^{-1}$  as seen in Figure 1(g,h). Interestingly, the scattering peak is smeared in the integration curve of the H-QD solid in Figure 1(i), indicating a successful short-range disorder configuration due to the homogeneous distribution of S-QDs and L-QDs, without the accumulation of monosized QDs. Notably, the H-QD solids exhibit similar GISAXS feature to QD solids made of “direct ink” with a broad QD size distribution.<sup>32,33</sup> The scattering similarity confirms our previous assumption about the peak smearing of interdot distance scattering of the direct ink-based QD solid.<sup>34</sup> A broadened size distribution (large particle radius standard deviation) is helpful to increase the packing density of the hard spheres model,<sup>35,36</sup> which can be used to explain the packing dynamics of the direct ink and the H-QDs. Notably, using H-QDs brings a very simplified method to modulate the packing dynamics of the QD HTL toward releasing the strains from monosized QDs and reducing film cracks. More importantly, previous efforts, including hybrid ligands, pretreatment, etc. could also be concluded in such principle, by partially introducing short-range disorder, such as different sizes, or different shapes, during the film fabrication process.<sup>27,37</sup> The as-formed long-range disorder can help boost the effective homogeneity and overall density of the QD HTLs.

Besides the structure study, we use photophysics methods to evaluate how the H-QDs influence the energy state distribution and the charge carrier dynamics of the QD HTLs, and the results are shown in Figure 2. The PL spectra of all compared QD HTLs are seen in Figure 2(a). Monosize QD solids exhibit featured PL peak positions from their band-edge radiative recombination at around 1150 nm for S-QDs and 1310 nm for L-QDs. Interestingly, H-QD solids exhibit enhanced PL intensities in different ratios in weight of S-QDs to L-QDs (S/L), in which the QD HTL with a ratio of S/L = 2:1 demonstrates the most prominent PL intensity as indicated by the pink curve. Two main factors contributing to the PL enhancement of the H-QD HTL are discussed below. The reduction of cracks in the QD HTLs by mixing QDs decreases the overall interface area and thus reduces the surface trap states, including the deep states for radiative recombination. Moreover, L-QDs surrounded by S-QDs become recombination centers for all nearby charge carriers, rather than facilitating charge carrier diffusion.

Figure 2(b) shows the TRPL data of all compared QD HTLs in a nonquench condition (on glass substrates).<sup>38</sup> We use a biexponential decay function to fit the data with parameters are seen in Table S1, in which  $\tau_2$  is assigned to be the factor relating to the surface trap states. We find that the QD HTL with S/L = 2:1 demonstrates the largest  $\tau_2$  value and the longest charge carrier lifetime, indicating the fewest trap density. Figure 2(c) shows the absorption spectra of the HTLs, where the first exciton absorption peak is clearly distinguishable in both monosize QD HTLs and H-QD HTLs. This suggests that the QDs maintain their absorption independence in mixed and strongly coupled QD stacking configurations.

To evaluate charge carrier transport in practical devices, we also use photophysics methods and investigate the charge carrier dynamics of QD HTLs on QD active layers, in which QD HTLs are respectively made of S-QDs, L-QDs, and H-QDs. The QD active layer is fabricated using the QD ink method, as described in the experimental section. The PL spectra of the compared active layers with different-size QD HTLs are shown in Figure 2(d). We find that charge carrier transfer from the S-QD HTL to the active layer is less efficient than that from the H-QD HTL, as indicated by the absence of the PL feature from the S-QDs. Nonetheless, the charge carrier transfer from S-QDs to the QD active layer is mostly prohibited from the apparent double PL peak in longer wavelengths in the case of H-QDs on the active layer. This means that the H-QD HTL improves hole transfer from the active layer to HTL, particularly to large QDs, which is confirmed by the TRPL data by tracking the PL lifetime of the active layer at around 1520 nm in Figure 2(e) and Table S2. The red shift of PL peak of QD active layer compared to the QDs in solvent is due to the partially aggregation.<sup>39,40</sup> Thus, all active layers were made in the same condition to ensure a

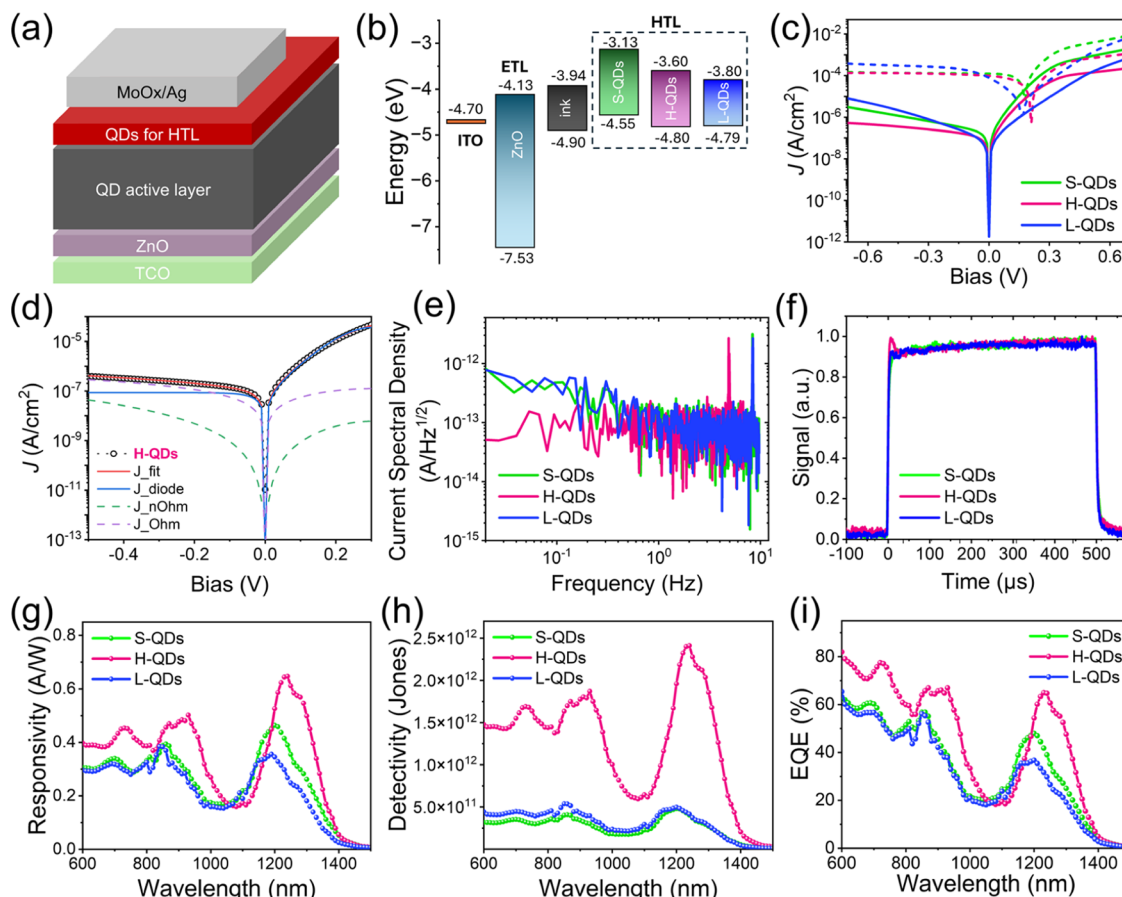


**Figure 4.** (a) Device architecture of the QD-SWIR photodetector. (b) Energy level alignment diagram of the p-i-n structure with HTLs made from QDs of different sizes. (c)  $J$ - $V$  characteristics for all QD devices. (d)  $J$ - $V$  curve fit of the dark current for the H-QD device (eq 2). (e) Noise current spectra for devices with different-sized QD HTLs. (f) On–off behavior. (g) Responsivity, (h) detectivity, and (i) EQE spectra for all devices with varying QD HTL sizes.

uniformed PL position to reduce the influence from the intrinsic active layers. The H-QD configuration exhibits a shorter average charge carrier lifetime than the S-QD configuration. Consequently, we briefly describe the improvement schematic of the HTL made of the H-QDs, as shown in Figure 2(f), in which the L-QDs in H-QDs play an important role in efficiently extracting holes from the active layer.

Single charge carrier devices based on monosize QD and H-QDs are fabricated to evaluate the trap density of the QD HTLs. The device architecture is shown in Figure 3(a) and the derived  $J$ - $V$  characters are shown in Figure 3(b). The trap-filled limit voltages ( $V_{TFL}$ ) are further fitted from the  $J$ - $V$  curves and the trap densities ( $n_t$ ) are estimated according to eq 1

$$n_t = 2\epsilon\epsilon_0 V_{TFL}/ed^2 \quad (1)$$

in which the  $\epsilon$  and  $\epsilon_0$  are relative primitivity and vacuum primitivity respectively.  $e$  is the elementary charge, and the  $d$  is the distance of the electrode. The H-QD HTL exhibits the smallest  $V_{TFL}$  (0.54 V) indicating the lowest trap state density, in good agreement with the TRPL data of the QD HTLs in the nonquench condition, in Figure 2(b). The trap states are assumed distributed on the solid surfaces as illustrated in Figure 3(c), in which the H-QDs exhibit the smallest effective surface under noncrack conditions. Moreover, we assume the H-QDs are better passivated due to their denser packing and

more homogeneous distribution, which reduces inner cracks compared to monosize QDs.

Further, we use the H-QDs to make HTLs in photodetector device fabrication to verify the benefits of H-QDs with different sizes. The photodetector device architecture is shown in Figure 4(a). It consists of a transport conductive oxide (TCO) layer as the bottom electrode, a ZnO electron transport layer (ETL), a QD solid active layer fabricated by solution-phase ligand exchange, and H-QDs as the HTL. A MoO<sub>x</sub> buffer layer is added as an additional HTL, with a silver top electrode. The energy band landscapes of the function layers of the device with different HTLs are shown in Figure 4(b), based on ultraviolet photoelectron spectroscopy (UPS) analysis (Figure S4). The H-QD HTL exhibits an intermediate energy band structure compared to S-QDs and L-QDs. In working devices, the S-QD HTL reduces charge carrier extraction by forming an energy barrier due to Fermi level alignment, while the L-QD HTL exhibits weak electron blocking. Interestingly, the H-QD HTL can reduces the barrier while still blocking electron transport. The  $J$ - $V$  characters of the devices from the same batch device fabrication in dark conditions and light conditions are shown in Figure 4(c), we find that the H-QD HTL device exhibits a better reverse saturation current characteristic with a reduced dark current density, compared to monosize QD HTL. This finding is mainly attributed to the synergic improvements from the energy band landscape and crack-free film morphology of the

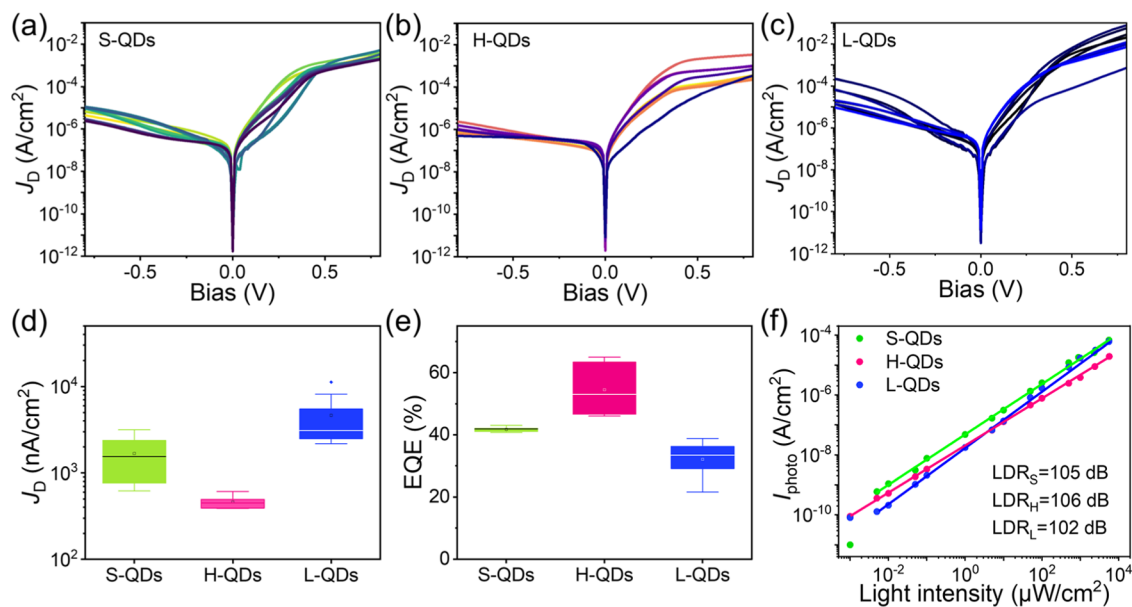


**Figure 5.**  $J$ - $V$  curves of 30 devices with (a) S-QD HTLs, (b) H-QD HTLs, and (c) L-QD HTLs. (d) Statistics of the dark current density of the devices at bias =  $-0.5$  V. (e) Statistics of the device EQE. (f) LDR of the champion devices made of different HTLs.

HTL. H-QD HTL thus reduces the leakage current from ohmic contact, which is studied by eq 2

$$J_D = J_0 \left( e^{\frac{e}{nk_B T}(V - J_D R_S)} - 1 \right) + \frac{V - J_D R_S}{R_{SH}} + k(V - J_D R_S)^m \quad (2)$$

Here  $J_D$  represents the dark current density of the device,  $V$  is the applied bias, and  $J_0$  for the reverse saturation current density of the diode.  $R_S$  and  $R_{SH}$  denote the series resistance and shunt resistance of the device, respectively.  $n$  is the diode ideality factor,  $k$  is the defect level, and  $m$  represents the defect concentration.<sup>3,14,41</sup> Notably, the ideality factor  $n = 1.4$  and power factor  $m = 2.4$  are determined according to literature considering that we focused on separating the leaking current under reverse bias into three different components including (i) diode current, (ii) ohmic current, and (iii) nonohmic current contributions.<sup>42,43</sup> The  $J$ - $V$  fitting results of H-QD device are shown in Figure 4(d) and the rest results are shown in Figure S6. The fitting parameters and results are provided in Tables S3 and S4. The device based on H-QD HTL with S/L = 2:1 of small QDs to large QDs exhibits the lowest dark current density of 392 nA/cm<sup>2</sup> in which the contribution from the ohmic contact ( $J_{\text{Ohm}}$ ) is significantly depressed to 285 nA/cm<sup>2</sup>. Notably, when the hybrid ratio of QDs is S/L = 1:1, the unexpected current contribution from the trap states is almost prohibited. Thus, the mixing QDs configuration effectively reduces the trap assisted tunneling from the  $J_{\text{non-Ohm}}$  comparison,<sup>44,45</sup> which agrees with the TRPL data and single-charge carrier device analysis. The results of frequency dependent current test are shown in Figure 4(e). The compared devices exhibit similar currents at  $f = 1$  Hz and bias = 0 V.

The response speed test results are seen in Figure 4(f) and the analysis are shown in Figure S8 and Table S6. H-QD HTL boosts the photodetector's response speed, which is attributed to a faster charge carrier mobility of the H-QD HTL than the monosize QD HTL. Specifically, the short-range disorder induced by H-QDs can enhance charge carrier mobility, consistent with previous studies,<sup>46,47</sup> which attribute this effect

primarily to the closer packing density observed through GISAXS. However, according to the Bässler equation,<sup>48,49</sup> charge carrier mobility is expected to decrease in H-QDs due to energy state disorder, as charge carriers tend to hop to sites with lower energy states and reduced interdot distance. Nonetheless, the increased packing density and reduced trap states in H-QDs can also enhance overall charge carrier mobility. This synergistic effect not only increases charge carrier diffusivity but may also create new transport pathways within the QD solid.<sup>50–52</sup> Briefly, in our case, the H-QDs-based structure disorder overwhelms the energetic disorder and brings a positive influence to the charge carrier mobility.

The spectra for responsivity ( $R$ ), detectivity ( $D^*$ ) and EQE are shown in Figure 4(g–i). The responsivity of the device is calculated based on eq 3

$$R = \frac{J_{\text{ph}}}{L_{\text{light}}} = \frac{I_{\text{light}} - I_{\text{dark}}}{P_{\text{hv}}} \quad (3)$$

in which  $J_{\text{ph}}$  and  $L_{\text{light}}$  respectively represent the light-generated light current density and the incident light power density.  $I_{\text{light}}$  and  $I_{\text{dark}}$  are the corresponding currents of the device in different test conditions, in specific light illumination, and under dark.  $P_{\text{hv}}$  is the light power of the incidence light with a frequency of  $\nu$  on the work area of the device. We confirm that H-QD HTL brings the device a very high responsivity of  $R = 0.65 \text{ A/W}$  at 1240 nm, which is much higher than that of devices with monosize QD HTLs, specifically,  $R = 0.46 \text{ A/W}$  for the S-QDs and  $R = 0.35 \text{ A/W}$  for the L-QDs, at 1200 nm. Besides, the detectivity ( $D^*$ ) of the device is calculated based on eq 4

$$D^* = \frac{(A\Delta f)^{1/2} R_\lambda}{i_n} \quad (4)$$

in which the  $A$  stands for the working area.  $f$  is the test current frequency of 1 Hz.  $R_\lambda$  is the responsivity at specific wavelength  $\lambda$  calculated from eq 2, and  $i_n$  is the noise current obtained from the noise spectral current in Figure 4(e). The device based on H-QD HTL exhibits an improved  $D^* = 2.4 \times 10^{12}$

jones (at 1240 nm, the peak position) compared to devices based on monosize QD HTL with the highest  $D^* = 5.0 \times 10^{11}$  jones at 1200 nm.

The external quantum efficiency (EQE) of the devices is calculated based on eq 5

$$\text{EQE} = \frac{hc}{\lambda} R \quad (5)$$

in which  $h$  stands for the plank constant,  $c$  for the light speed, and  $\lambda$  for the wavelength respectively. The H-QD HTL SWIR photodetector exhibits over 65% EQE at 1240 nm, which is much higher than devices based on monosize QDs (48% for S-QD HTL device, 37% for L-QD HTL device at 1200 nm). In addition, a device comparison table is prepared as seen in Table S9 which indicates our champion device based on H-QD HTL outperforms most recent devices with state-of-the-art in literature.

Figure 5(a–c) show the  $J$ – $V$  characters of 30 compared devices with optimized ZnO ETL layers in a dark condition. Figure 5(d) illustrates the statistics of the dark current density of the devices at bias = −0.5 V. The QD-PD devices with H-QD HTLs exhibit apparently depressed dark current density (minimum  $J_D = 388 \text{ nA/cm}^2$ ) compared to the devices with monosize QD HTLs, minimum  $J_D = 620 \text{ nA/cm}^2$  for S-QD devices and minimum  $J_D = 2175 \text{ nA/cm}^2$  for L-QD devices. Besides, the statistics of the EQE of the compared devices as shown in Figure 5(e) indicate the priority of the devices with H-QD HTLs. Specifically, the average EQE = 54% for the H-QD devices, 41% for the S-QD devices and 33% for the L-QD devices. Besides, the linear dynamic ranges (LDRs) of the champion devices for comparison are shown in Figure 5(f). The device with the H-QD HTL demonstrates a broader LDR than the rest champion devices with monosize QD HTLs.

## CONCLUSIONS

In conclusion, we demonstrate that short-range disorder stacking in QDs within solid-state HTLs can be effectively achieved by mixing QDs of different sizes during HTL fabrication via SSLE. Surface morphology analysis confirms a crack-free structure, while GISAXS measurements show a denser packing density in the solid composed of hybrid-size QDs. We discuss the stacking kinetics in detail, showing that a broadened, modulated size distribution of QDs results in a more compact packing. Photophysical studies suggest that H-QDs optimize charge carrier dynamics in the QD HTL, leading to improved hole extraction compared to monosize QDs. Additionally, single charge carrier device analysis reveals a reduction in trap density with H-QDs. As a result, QD SWIR photodetectors incorporating the H-QD HTL outperform those using monosize QD HTLs. By mixing QDs in a small-to-large ratio of 2:1 by weight, the dark current density is reduced to 392  $\text{nA/cm}^2$ , primarily due to the suppression of leakage current from ohmic contact. In addition, the device shows improved performance with a responsivity of 0.65 A/W, detectivity of  $2.4 \times 10^{12}$  Jones, and an external quantum efficiency (EQE) of 65% in the SWIR region. These results demonstrate that mixing different-sized QDs improves film quality and optimizes the electronic properties of the QD HTL, thereby offering a promising route for fabricating high-performance QD SWIR detectors and imagers.

## ASSOCIATED CONTENT

### Supporting Information

The Supporting Information is available free of charge at <https://pubs.acs.org/doi/10.1021/acsphtronics.4c01864>.

Experimental section, basic properties of as-prepared PbS QDs include TEM, absorption spectra; SEM images, UPS data and TR-PL parameters of the QD solids; QD SWIR device photograph and device working area, fitting curves and parameters of the QD devices; EQE of the devices under bias; response speed test results;  $J$ – $V$  simulations; comparison table of the device performance ([PDF](#))

## AUTHOR INFORMATION

### Corresponding Authors

**Haodong Tang** – College of Integrated Circuits and Optoelectronic Chips, Shenzhen Technology University, Shenzhen 518118, China; Email: [tanghaodong@sztu.edu.cn](mailto:tanghaodong@sztu.edu.cn)

**Peter Müller-Buschbaum** – Department of Physics, Chair for Functional Materials, Technical University of Munich, TUM School of Natural Sciences, 85748 Garching, Germany; [orcid.org/0000-0002-9566-6088](https://orcid.org/0000-0002-9566-6088); Email: [mueller@ph.tum.de](mailto:mueller@ph.tum.de)

**Kai Wang** – Institute of Nanoscience and Applications, Department of Electronic and Electrical Engineering, Southern University of Science and Technology, Shenzhen 518055, China; [orcid.org/0000-0003-0443-6955](https://orcid.org/0000-0003-0443-6955); Email: [wangk@sustech.edu.cn](mailto:wangk@sustech.edu.cn)

**Wei Chen** – Shenzhen Key Laboratory of Ultraintense Laser and Advanced Material Technology, Center for Intense Laser Application Technology, and College of Engineering Physics, Shenzhen Technology University, Shenzhen 518118, China; [orcid.org/0000-0001-9550-0523](https://orcid.org/0000-0001-9550-0523); Email: [chenwei@sztu.edu.cn](mailto:chenwei@sztu.edu.cn)

### Authors

**Simin Chen** – Shenzhen Key Laboratory of Ultraintense Laser and Advanced Material Technology, Center for Intense Laser Application Technology, and College of Engineering Physics, Shenzhen Technology University, Shenzhen 518118, China; College of Integrated Circuits and Optoelectronic Chips, Shenzhen Technology University, Shenzhen 518118, China; School of Materials Science and Engineering, Hubei University, Wuhan 430062, China

**Huaying Zhong** – Shenzhen Key Laboratory of Ultraintense Laser and Advanced Material Technology, Center for Intense Laser Application Technology, and College of Engineering Physics, Shenzhen Technology University, Shenzhen 518118, China; Department of Physics, Chair for Functional Materials, Technical University of Munich, TUM School of Natural Sciences, 85748 Garching, Germany; [orcid.org/0000-0002-3882-4131](https://orcid.org/0000-0002-3882-4131)

**Xiao Wang** – Shenzhen Key Laboratory of Ultraintense Laser and Advanced Material Technology, Center for Intense Laser Application Technology, and College of Engineering Physics, Shenzhen Technology University, Shenzhen 518118, China; School of Materials Science and Engineering, Hubei University, Wuhan 430062, China

**Guangjiu Pan** – Department of Physics, Chair for Functional Materials, Technical University of Munich, TUM School of

Natural Sciences, 85748 Garching, Germany;  orcid.org/0000-0001-9187-6267

Fan Fang – Shenzhen Key Laboratory of Ultraintense Laser and Advanced Material Technology, Center for Intense Laser Application Technology, and College of Engineering Physics, Shenzhen Technology University, Shenzhen 518118, China

Jiufeng Wu – Shenzhen Key Laboratory of Ultraintense Laser and Advanced Material Technology, Center for Intense Laser Application Technology, and College of Engineering Physics, Shenzhen Technology University, Shenzhen 518118, China

Weichao Wang – School of Materials Science and Engineering, Hubei University, Wuhan 430062, China;  orcid.org/0009-0000-7716-9427

Lihai Xu – School of Materials Science and Engineering, Hubei University, Wuhan 430062, China

Jun Tang – College of New Materials and New Energies, Shenzhen Technology University, Shenzhen 518118, China;  orcid.org/0000-0001-6229-2051

Junjie Hao – College of Integrated Circuits and Optoelectronic Chips, Shenzhen Technology University, Shenzhen 518118, China;  orcid.org/0000-0002-1345-8761

Keyu Zheng – School of Materials Science and Engineering, Hubei University, Wuhan 430062, China

Dan Wu – College of New Materials and New Energies, Shenzhen Technology University, Shenzhen 518118, China

Zeguo Tang – College of New Materials and New Energies, Shenzhen Technology University, Shenzhen 518118, China

Lei Zhang – School of Materials Science and Engineering, Hubei University, Wuhan 430062, China

Leifeng Cao – Shenzhen Key Laboratory of Ultraintense Laser and Advanced Material Technology, Center for Intense Laser Application Technology, and College of Engineering Physics, Shenzhen Technology University, Shenzhen 518118, China

Complete contact information is available at:

<https://pubs.acs.org/10.1021/acsphtronics.4c01864>

## Author Contributions

▀S.C., H.Z., and X.W. contributed equally to this work. S.C.: Data curation, investigation, formal analysis. H.Z.: Data curation, investigation. X.W.: Data curation, visualization. G.P.: Data curation, visualization. H.T.: Supervision, visualization, investigation. F.F.: Formal analysis. J.W.: Investigation. W.W.: Investigation. L.X.: Validation. J.T.: Resources. J.H.: Resources. K.Z.: Resources. D.W.: Resources, investigation. Z.T.: Resources, investigation. L.Z.: Methodology, investigation. L.C.: Resources. P.M.-B.: Supervision, methodology, writing—review and editing. K.W.: Supervision, investigation, writing—review and Editing. W.C.: Conceptualization, investigation, supervision, funding acquisition, writing—original draft.

## Funding

This work is supported by the National Natural Science Foundation of China (Nos. 12204318, 62204107, 51825301, 62122034, 62261136552), Shenzhen Science and Technology Program (Nos. R CYX20221008092908030, ZDSYS20200811143600001), Natural Science Foundation of Top Talent of SZTU (Nos. GDRC202340, GDRC202345). K.W. acknowledges funding support from High Level of Special Funds (Nos. G030230001, G03034K002) from Southern University of Science and Technology. H.Z. and G.P. acknowledge the financial support from the China Scholarship Council (CSC). P.M.-B. acknowledges the funding

from the Deutsche Forschungsgemeinschaft (DFG, German Research Foundation) under Germany's Excellence Strategy—EXC 2089/1–390776260 (e-conversion) and from TUM.solar in the context of the Bavarian Collaborative Research Project Solar Technologies Go Hybrid (SolTech).

## Notes

The authors declare no competing financial interest.

## ■ REFERENCES

- (1) Li, F.; Liu, J. J.; Xu, Q.; Chang, R.; Wang, L.; Wu, Z.; Shen, H.; Du, Z. High-Radiance Shortwave Infrared Light-Emitting Diodes Based on Highly Stable PbS Colloidal Quantum Dots. *J. Phys. Chem. Lett.* **2023**, *14* (18), 4252–4258.
- (2) Gong, M.; Li, F.; Wang, L.; Xu, Q.; Wu, Z.; Shen, H.; Li, L. S.; Du, Z. Highly Monodisperse PbS Quantum Dots with Facet Engineering for High-Radiance Light-Emitting Diodes in the NIR-II Window. *ACS Photonics* **2023**, *10* (7), 2241–2248.
- (3) Wang, Y.; Peng, L.; Schreier, J.; Bi, Y.; Black, A.; Malla, A.; Goossens, S.; Konstantatos, G. Silver telluride colloidal quantum dot infrared photodetectors and image sensors. *Nat. Photonics* **2024**, *18* (3), 236–242.
- (4) Wang, H.; Pinna, J.; Romero, D. G.; Di Mario, L.; Koushki, R. M.; Kot, M.; Portale, G.; Loi, M. A. PbS Quantum Dots Ink with Months-Long Shelf-Lifetime Enabling Scalable and Efficient Short-Wavelength Infrared Photodetectors. *Adv. Mater.* **2024**, *36* (19), No. e2311526.
- (5) Li, M.; Zhao, X.; Zhang, A.; Wang, B.; Yang, Y.; Xu, S.; Hu, Q.; Liang, G.; Xiao, Z.; Gao, L.; Zhang, J.; Hsu, H.-Y.; Song, H.; Tang, J. Organic ligand complementary passivation to Colloidal-quantum-dot surface enables efficient infrared solar cells. *Chem. Eng. J.* **2023**, *455*, 140961.
- (6) Yang, Q.; Huang, H.-W.; Xu, G.; Yuan, Y.; Jiang, M.-T.; Zhong, Y.-N.; Gao, X.; Xu, J.-L.; Wang, S.-D. Self-formed interfacial oxide layer minimizes reverse bias dark current in PbS colloidal quantum dot photodiodes. *Appl. Phys. Lett.* **2023**, *123* (21), 213302.
- (7) Ding, C.; Wang, D.; Liu, D.; Li, H.; Li, Y.; Hayase, S.; Sogabe, T.; Masuda, T.; Zhou, Y.; Yao, Y.; Zou, Z.; Wang, R.; Shen, Q. Over 15% Efficiency PbS Quantum-Dot Solar Cells by Synergistic Effects of Three Interface Engineering: Reducing Nonradiative Recombination and Balancing Charge Carrier Extraction. *Adv. Energy Mater.* **2022**, *12* (35), No. 2201676.
- (8) Vafaei, M.; Fan, J. Z.; Morteza Najarian, A.; Ouellette, O.; Sagar, L. K.; Bertens, K.; Sun, B.; García de Arquer, F. P.; Sargent, E. H. Colloidal quantum dot photodetectors with 10-ns response time and 80% quantum efficiency at 1,550 nm. *Matter* **2021**, *4* (3), 1042–1053.
- (9) Gregory, C.; Hilton, A.; Violette, K.; Klem, E. J. D. Colloidal Quantum Dot Photodetectors for Large Format NIR, SWIR, and eSWIR Imaging Arrays. In *SID Symposium Digest of Technical Papers* 2021; pp 982–986.
- (10) Liu, J.; Liu, P.; Chen, D.; Shi, T.; Qu, X.; Chen, L.; Wu, T.; Ke, J.; Xiong, K.; Li, M.; Song, H.; Wei, W.; Cao, J.; Zhang, J.; Gao, L.; Tang, J. A near-infrared colloidal quantum dot imager with monolithically integrated readout circuitry. *Nat. Electronics* **2022**, *5* (7), 443–451.
- (11) Pejovic, V.; Georgitzikis, E.; Lee, J.; Lieberman, I.; Cheyns, D.; Heremans, P.; Malinowski, P. E. Infrared Colloidal Quantum Dot Image Sensors. *IEEE Trans. Electron Devices* **2022**, *69* (6), 2840–2850.
- (12) Malinowski, P. E.; Pejovic, V.; Georgitzikis, E.; Kim, J. H.; Lieberman, I.; Papadopoulos, N.; Lim, M. J.; Hagelsieb, L. M.; Chandrasekaran, N.; Puybaret, R.; Li, Y.; Verschooten, T.; Thijs, S.; Cheyns, D.; Heremans, P.; Lee, J. Colloidal Quantum Dot Image Sensors: A New Vision for Infrared. In *2022 International Electron Devices Meeting (IEDM)*; IEEE: San Francisco, CA, USA, 2022; p 19.
- (13) Brown, P. R.; Kim, D.; Lunt, R. R.; Zhao, N.; Bawendi, M. G.; Grossman, J. C.; Bulović, V. Energy Level Modification in Lead Sulfide Quantum Dot Thin Films through Ligand Exchange. *ACS Nano* **2014**, *8* (6), 5863–5872.

- (14) Wang, Y.; Hu, H.; Yuan, M.; Xia, H.; Zhang, X.; Liu, J.; Yang, J.; Xu, S.; Shi, Z.; He, J.; Zhang, J.; Gao, L.; Tang, J.; Lan, X. Colloidal PbS Quantum Dot Photodiode Imager with Suppressed Dark Current. *ACS Appl. Mater. Interfaces* **2023**, *15* (50), 58573–58582.
- (15) Chuang, C.-H. M.; Brown, P. R.; Bulović, V.; Bawendi, M. G. Improved performance and stability in quantum dot solar cells through band alignment engineering. *Nat. Mater.* **2014**, *13* (8), 796–801.
- (16) Shi, G.; Kaewprajak, A.; Ling, X.; Hayakawa, A.; Zhou, S.; Song, B.; Kang, Y.; Hayashi, T.; Altun, M. E.; Nakaya, M.; Liu, Z.; Wang, H.; Sagawa, T.; Ma, W. Finely Interpenetrating Bulk Heterojunction Structure for Lead Sulfide Colloidal Quantum Dot Solar Cells by Convective Assembly. *ACS Energy Lett.* **2019**, *4* (4), 960–967.
- (17) Chen, Z.; Huang, T.; Zhang, B.; Wu, C.; Zhang, X.; Sun, T.; Xu, W.; Kang, K.; Xiang, C.; Zhang, T.; Li, R. Suppression of the dark current in PbS quantum dot infrared photodetectors through the introduction of a CuInSeS interfacial layer. *J. Mater. Chem. C* **2024**, *12* (12), 4493–4500.
- (18) Kirmani, A. R.; Sheikh, A. D.; Niazi, M. R.; Haque, M. A.; Liu, M.; de Arquer, F. P. G.; Xu, J.; Sun, B.; Voznyy, O.; Gasparini, N.; Baran, D.; Wu, T.; Sargent, E. H.; Amassian, A. Overcoming the Ambient Manufacturability-Scalability-Performance Bottleneck in Colloidal Quantum Dot Photovoltaics. *Adv. Mater.* **2018**, *30* (35), No. e1801661.
- (19) Klem, E. J. D.; Shukla, H.; Hinds, S.; MacNeil, D. D.; Levina, L.; Sargent, E. H. Impact of dithiol treatment and air annealing on the conductivity, mobility, and hole density in PbS colloidal quantum dot solids. *Appl. Phys. Lett.* **2008**, *92* (21), No. 212105.
- (20) Wang, C.; Wu, Q.; Wang, Y.; Wang, Z.; Li, H.; Li, X.; Chen, X.; Wang, C.; Liu, Y.; Zhang, X. P-Type PbS Quantum Dot Solar Ink via Hydrogen-Bonding Modulated Solvation for High-Efficiency Photovoltaics. *Adv. Funct. Mater.* **2024**, *34* (18), 2315365 DOI: [10.1002/adfm.202315365](https://doi.org/10.1002/adfm.202315365).
- (21) Sharma, A.; Dambhare, N. V.; Bera, J.; Sahu, S.; Rath, A. K. Crack-Free Conjugated PbS Quantum Dot–Hole Transport Layers for Solar Cells. *ACS Appl. Nano Mater.* **2021**, *4* (4), 4016–4025.
- (22) Huang, T.; Wu, C.; Yang, J.; Hu, P.; Qian, L.; Sun, T.; Xiang, C. Reducing the Open-Circuit Voltage Loss of PbS Quantum Dot Solar Cells via Hybrid Ligand Exchange Treatment. *ACS Appl. Mater. Interfaces* **2024**, *16* (1), 915–923.
- (23) Chen, W.; Tang, H.; Li, N.; Scheel, M. A.; Xie, Y.; Li, D.; Körstgens, V.; Schwartzkopf, M.; Roth, S. V.; Wang, K.; Sun, X. W.; Müller-Buschbaum, P. Colloidal PbS quantum dot stacking kinetics during deposition via printing. *Nanoscale Horizons* **2020**, *5* (5), 880–885.
- (24) Septianto, R. D.; Miranti, R.; Kikitsu, T.; Hikima, T.; Hashizume, D.; Matsushita, N.; Iwasa, Y.; Bisri, S. Z. Enabling metallic behaviour in two-dimensional superlattice of semiconductor colloidal quantum dots. *Nat. Commun.* **2023**, *14* (1), 2670.
- (25) Cimada daSilva, J.; Balazs, D. M.; Dunbar, T. A.; Hanrath, T. Fundamental Processes and Practical Considerations of Lead Chalcogenide Mesocrystals Formed via Self-Assembly and Directed Attachment of Nanocrystals at a Fluid Interface. *Chem. Mater.* **2021**, *33* (24), 9457–9472.
- (26) Chen, W.; Zhong, J.; Li, J.; Saxena, N.; Kreuzer, L. P.; Liu, H.; Song, L.; Su, B.; Yang, D.; Wang, K.; Schlipf, J.; Körstgens, V.; He, T.; Wang, K.; Müller-Buschbaum, P. Structure and Charge Carrier Dynamics in Colloidal PbS Quantum Dot Solids. *J. Phys. Chem. Lett.* **2019**, *10* (9), 2058–2065.
- (27) Lu, K.; Meng, X.; Liu, Z.; Chen, J.; Wang, Y.; Zhang, Y.; Zhang, X.; Sarnello, E.; Shi, G.; Patil, R. P.; Deng, W.; Zhou, S.; Gu, M.; Zhong, Y.; Jeong, S.; Gu, X. W.; Li, T.; Ye, X.; Ma, W. Packing State Management to Realize Dense and Semiconducting Lead Sulfide Nanocrystals Film via a Single-Step Deposition. *Cell Rep. Phys. Sci.* **2020**, *1* (9), No. 100183.
- (28) Corricelli, M.; Altamura, D.; De Caro, L.; Guagliardi, A.; Falqui, A.; Genovese, A.; Agostiano, A.; Giannini, C.; Striccoli, M.; Curri, M. L. Self-organization of mono- and bi-modal PbS nanocrystal populations in superlattices. *CrystEngComm* **2011**, *13* (12), 3988.
- (29) Corricelli, M.; Enrichi, F.; Altamura, D.; De Caro, L.; Giannini, C.; Falqui, A.; Agostiano, A.; Curri, M. L.; Striccoli, M. Near Infrared Emission from Monomodal and Bimodal PbS Nanocrystal Superlattices. *J. Phys. Chem. C* **2012**, *116* (10), 6143–6152.
- (30) Biondi, M.; Choi, M.-J.; Lee, S.; Bertens, K.; Wei, M.; Kirmani, A. R.; Lee, G.; Kung, H. T.; Richter, L. J.; Hoogland, S.; Lu, Z.-H.; García de Arquer, F. P.; Sargent, E. H. Control Over Ligand Exchange Reactivity in Hole Transport Layer Enables High-Efficiency Colloidal Quantum Dot Solar Cells. *ACS Energy Lett.* **2021**, *6* (2), 468–476.
- (31) Chen, W.; Tang, H.; Chen, Y.; Heger, J. E.; Li, N.; Kreuzer, L. P.; Xie, Y.; Li, D.; Anthony, C.; Pikramenou, Z.; Ng, K. W.; Sun, X. W.; Wang, K.; Müller-Buschbaum, P. Spray-deposited PbS colloidal quantum dot solid for near-infrared photodetectors. *Nano Energy* **2020**, *78*, 105254.
- (32) Liu, Y.; Gao, Y.; Yang, Q.; Xu, G.; Zhou, X.; Shi, G.; Lyu, X.; Wu, H.; Liu, J.; Fang, S.; Ullah, M. I.; Song, L.; Lu, K.; Cao, M.; Zhang, Q.; Li, T.; Xu, J.; Wang, S.; Liu, Z.; Ma, W. Breaking the Size Limitation of Directly-Synthesized PbS Quantum Dot Inks Toward Efficient Short-wavelength Infrared Optoelectronic Applications. *Angew. Chem., Int. Ed.* **2023**, *62* (17), No. e202300396.
- (33) Wang, Y.; Liu, Z.; Huo, N.; Li, F.; Gu, M.; Ling, X.; Zhang, Y.; Lu, K.; Han, L.; Fang, H.; Shulga, A. G.; Xue, Y.; Zhou, S.; Yang, F.; Tang, X.; Zheng, J.; Antonietta Loi, M.; Konstantatos, G.; Ma, W. Room-temperature direct synthesis of semi-conductive PbS nanocrystal inks for optoelectronic applications. *Nat. Commun.* **2019**, *10* (1), No. 5136.
- (34) Li, F.; Liu, Y.; Shi, G.; Chen, W.; Guo, R.; Liu, D.; Zhang, Y.; Wang, Y.; Meng, X.; Zhang, X.; Lv, Y.; Deng, W.; Zhang, Q.; Shi, Y.; Chen, Y.; Wang, K.; Shen, Q.; Liu, Z.; Müller-Buschbaum, P.; Ma, W. Matrix Manipulation of Directly-Synthesized PbS Quantum Dot Inks Enabled by Coordination Engineering. *Adv. Funct. Mater.* **2021**, *31* (45), 2104457.
- (35) Desmond, K. W.; Weeks, E. R. Influence of particle size distribution on random close packing of spheres. *Phys. Rev. E* **2014**, *90* (2), No. 022204.
- (36) Baranau, V.; Tallarek, U. Random-close packing limits for monodisperse and polydisperse hard spheres. *Soft Matter* **2014**, *10* (21), 3826–3841.
- (37) Liu, L.; Yuan, Y.; Deng, W.; Li, S. Determining random packing density and equivalent packing size of superballs via binary mixtures with spheres. *Chem. Eng. Sci.* **2019**, *202*, 270–281.
- (38) Lee, E. M. Y.; Tisdale, W. A. Determination of Exciton Diffusion Length by Transient Photoluminescence Quenching and Its Application to Quantum Dot Films. *J. Phys. Chem. C* **2015**, *119* (17), 9005–9015.
- (39) Shi, G.; Wang, H.; Zhang, Y.; Cheng, C.; Zhai, T.; Chen, B.; Liu, X.; Jono, R.; Mao, X.; Liu, Y.; Zhang, X.; Ling, X.; Zhang, Y.; Meng, X.; Chen, Y.; Duhm, S.; Zhang, L.; Li, T.; Wang, L.; Xiong, S.; Sagawa, T.; Kubo, T.; Segawa, H.; Shen, Q.; Liu, Z.; Ma, W. The effect of water on colloidal quantum dot solar cells. *Nat. Commun.* **2021**, *12* (1), No. 4381.
- (40) Choi, J.; Choi, M. J.; Kim, J.; Dinic, F.; Todorovic, P.; Sun, B.; Wei, M.; Baek, S. W.; Hoogland, S.; Garcia de Arquer, F. P.; Voznyy, O.; Sargent, E. H. Stabilizing Surface Passivation Enables Stable Operation of Colloidal Quantum Dot Photovoltaic Devices at Maximum Power Point in an Air Ambient. *Adv. Mater.* **2020**, *32* (7), No. e1906497.
- (41) Yang, J.; Lu, S.; Xia, B.; Liu, P.; Yang, Y.; Xiao, Z.; Zhang, J.; Gao, L.; Tang, J. Excess PbBr<sub>2</sub> Passivation of Large PbS Colloidal Quantum Dots to Reduce Dark-Current Density for Near-Infrared Detection. *Phys. Rev. Appl.* **2023**, *19* (1), 014021.
- (42) Williams, B. L.; Smit, S.; Kniknie, B. J.; Bakkers, N. J.; Kessels, W. M. M.; Schropp, R. E. I.; Creatore, M. Identifying Parasitic Current Pathways in CIGS Solar Cells by Modelling Dark JV Response. *Prog. Photovolt.: Res. Appl.* **2015**, *23* (11), 1516–1525.
- (43) Chen, D.; Liu, Y.; Xia, B.; Chen, L.; Yang, Y.; Yang, G.; Liu, J.; Lu, S.; Ge, C.; Liu, P.; Yang, J.; Liang, G.; Lan, X.; Zeng, X.; Li, L.; Zhang, J.; Xiao, Z.; Gao, L.; Tang, J. Passivating {100} Facets of PbS Colloidal Quantum Dots via Perovskite Bridges for Sensitive and

- Stable Infrared Photodiodes. *Adv. Funct. Mater.* **2023**, *33* (1), 2210158.
- (44) Sandberg, O. J.; Sundqvist, A.; Nyman, M.; Österbacka, R. Relating Charge Transport, Contact Properties, and Recombination to Open-Circuit Voltage in Sandwich-Type Thin-Film Solar Cells. *Phys. Rev. Appl.* **2016**, *5* (4), 044005.
- (45) Yang, Q. K.; Fuchs, F.; Schmitz, J.; Pletschen, W. Investigation of trap-assisted tunneling current in InAs/(GaIn)Sb superlattice long-wavelength photodiodes. *Appl. Phys. Lett.* **2002**, *81* (25), 4757–4759.
- (46) Gilmore, R. H.; Lee, E. M. Y.; Weidman, M. C.; Willard, A. P.; Tisdale, W. A. Charge Carrier Hopping Dynamics in Homogeneously Broadened PbS Quantum Dot Solids. *Nano Lett.* **2017**, *17* (2), 893–901.
- (47) Lee, E. M. Y.; Tisdale, W. A.; Willard, A. P. Can Disorder Enhance Incoherent Exciton Diffusion? *J. Phys. Chem. B* **2015**, *119* (30), 9501–9509.
- (48) Wojcik, M.; Zawieja, I.; Seki, K. Charge Transport in Disordered Organic Solids: Refining the Bässler Equation with High-Precision Simulation Results. *J. Phys. Chem. C* **2020**, *124* (33), 17879–17888.
- (49) Xing, Y.; Yazdani, N.; Lin, W. M. M.; Yarema, M.; Zahn, R.; Wood, V. Effect of Positional Disorders on Charge Transport in Nanocrystal Quantum Dot Thin Films. *ACS Appl. Electron. Mater.* **2022**, *4* (2), 631–642.
- (50) Choi, M.-J.; García de Arquer, F. P.; Proppe, A. H.; Seifitokaldani, A.; Choi, J.; Kim, J.; Baek, S.-W.; Liu, M.; Sun, B.; Biondi, M.; Scheffel, B.; Walters, G.; Nam, D.-H.; Jo, J. W.; Ouellette, O.; Voznyy, O.; Hoogland, S.; Kelley, S. O.; Jung, Y. S.; Sargent, E. H. Cascade surface modification of colloidal quantum dot inks enables efficient bulk homojunction photovoltaics. *Nat. Commun.* **2020**, *11* (1), No. 103.
- (51) Gilmore, R. H.; Winslow, S. W.; Lee, E. M. Y.; Ashner, M. N.; Yager, K. G.; Willard, A. P.; Tisdale, W. A. Inverse Temperature Dependence of Charge Carrier Hopping in Quantum Dot Solids. *ACS Nano* **2018**, *12* (8), 7741–7749.
- (52) Lee, S.; Zhitomirsky, D.; Grossman, J. C. Manipulating Electronic Energy Disorder in Colloidal Quantum Dot Solids for Enhanced Charge Carrier Transport. *Adv. Funct. Mater.* **2016**, *26* (10), 1554–1562.

#### ■ NOTE ADDED AFTER ASAP PUBLICATION

This paper was originally published ASAP on January 2, 2025. Equation 2 was revised, and the paper reposted on January 24, 2025.



CAS BIOFINDER DISCOVERY PLATFORM™

**STOP DIGGING  
THROUGH DATA  
— START MAKING  
DISCOVERIES**

CAS BioFinder helps you find the right biological insights in seconds

Start your search

